micromachines

MDPI

Article

The Influence of Gap Angle on the Transport Characteristics of Split-Gate AlGaN/GaN Heterostructure Field-Effect Transistors

Ying Kang [1,2], Xiaojia Zhang [1,2], Guangyuan Jiang [1,2], Chen Fu [1,2], Zhenfei Hou [1,2], Guangyuan Zhang [1,2], Caina Luan [3] and Yang Liu [1,2,*]

[1] Shandong Key Laboratory of Technologies and Systems for Intelligent Construction Equipment, Shandong Jiaotong University, Jinan 250357, China
[2] School of Information Science and Electrical Engineering, Shandong Jiaotong University, Jinan 250357, China
[3] School of Integrated Circuits, Shandong University, Jinan 250100, China
* Correspondence: wdzliuyang@sdjtu.edu.cn

Abstract

In this work, split-gate (SG) AlGaN/GaN heterostructure field-effect transistors (HFETs) with different gap angles were fabricated. The effect of the gap angle on the transport characteristics of these SG devices was investigated via measurement and analysis of their direct-current electrical properties. The results show that varying the gap angle significantly influences the channel current and further modulates the turn-off voltage of the devices. Theoretical analysis indicated that a change in gap angle directly alters the length of the gap region and affects the conduction channel effective width (Weff) through geometric effects, thereby modifying the channel current. In addition, the gap angle affects the total amount and distribution of additional polarization charges underneath the gate, which influences the polarization Coulomb field (PCF) scattering intensity and thus modulates the electron mobility of the devices. These findings provide a new direction for the structural optimization of SG AlGaN/GaN HFETs and offer a valuable reference for further improving the performance of SG devices.

Keywords: AlGaN/GaN HFETs; split-gate; transport characteristics; PCF scattering

1. Introduction

Benefiting from GaN's outstanding properties, AlGaN/GaN heterostructure field-effect transistors (HFETs) possess a high breakdown voltage and large saturated electron drift velocity, making them well suited to high-frequency and high-power applications [1–6]. The split-gate (SG) structure was initially developed for AlGaAs/GaAs heterostructure devices and later extended to AlGaN/GaN counterparts [7–9]. Early studies mainly utilized the SG structure to construct quantum wires or quantum dots [10–13], but it has subsequently been explored as a modulation gate, yielding devices with distinctive performance [14–17]. Compared with standard AlGaN/GaN HFETs, SG devices have a wider voltage modulation range and lower threshold voltage [14]. When used as voltage amplifiers, they are expected to achieve high linear voltage amplification with lower power consumption [14,18,19]. Nevertheless, our understanding of SG AlGaN/GaN HFETs remains incomplete at present. The gap region, unique to SG AlGaN/GaN HFETs, serves as a conduction path between the source and drain regions after the pinch-off of the gated channel, and its geometry is expected to greatly affect carrier transport. However, there remains a lack of systematic investigations into how the geometry of this gap region affects the transport characteristics of SG AlGaN/GaN HFETs.

Check for updates

Academic Editor: Piero Malcovati

Received: 6 June 2026
Revised: 1 July 2026
Accepted: 10 July 2026
Published: 11 July 2026

Copyright: © 2026 by the authors. Licensee MDPI, Basel, Switzerland. This article is an open access article distributed under the terms and conditions of the Creative Commons Attribution (CC BY) license.

In this study, SG AlGaN/GaN HFETs with various gap angles were fabricated to tailor the geometry of the gap region. Electrical measurements confirmed that the gap angle significantly modulates the devices' channel current and turn-off voltage. Further theoretical analysis revealed that varying the gap angle not only alters the physical length of the gap itself but also affects the conduction channel effective width (W_{eff}) through geometric effects. The gap angle also affects channel electron mobility by influencing polarization Coulomb field (PCF) scattering. These results confirm that tailoring the gap geometry is an effective strategy to control the transport properties and optimize the performance of SG AlGaN/GaN HFETs.

2. Experiments

The AlGaN/GaN heterostructure material used in this study was prepared on a 1000 μm Si substrate via MOCVD; its layer configuration is presented in Figure 1. The buffer layer of the material was C-doped to compensate for background carriers and achieve high resistivity, while the channel and barrier layers were unintentionally doped. Hall measurements yielded a two-dimensional electron gas (2DEG) sheet density (n_{2D}) of roughly 1.06×10^{13} cm^{-2} and a Hall mobility of approximately 1936 cm^2/(V·s). Device isolation was accomplished through fluorine ion implantation. Source and drain contacts were formed by depositing a Ti/Al/Ni/Au (20 nm/130 nm/50 nm/50 nm) stack via electron-beam evaporation followed by rapid thermal annealing at 875 °C for 30 s in a nitrogen atmosphere to ensure ohmic behavior. The specific resistivity of the ohmic contacts was measured to be approximately 4.74×10^{-4} Ω·cm^2 via the transmission line method. The gate Schottky contact was realized by evaporating a Ni/Au (50 nm/150 nm) bilayer, and all device patterning was defined using ultraviolet photolithography during fabrication. Room-temperature electrical characterization was performed using an Agilent B1500A analyzer (Keysight Technologies Inc., Santa Rosa, CA, USA) for current–voltage (I-V) measurements and an Agilent B1520A unit (Keysight Technologies Inc., Santa Rosa, CA, USA) at 1 MHz for capacitance–voltage (C-V) measurements.

Six samples were fabricated and characterized according to the above process. Samples 1–3 are SG devices, the structures of which are shown in Figure 1a, while samples 4–6 are hollow-split-gate (HSG) devices, as illustrated in Figure 1b. In each sample, there is a gap in the middle of the two gates. The dimensional parameters of each sample are listed in detail in Table 1. As can be seen from Figure 1 and Table 1, samples 1 and 4 have identical structures and dimensions, differing only in whether the structure of the gate is hollow. The same relationship applies to samples 2 and 5, as well as samples 3 and 6. Therefore, at the gate pinch-off point, the W_{eff} values of samples 1–3 are equal to those of samples 4–6, respectively [20]. In this work, the measurement data for samples 4–6 are used only for the quantitative analysis of W_{eff}; all other analyses are based on data from samples 1–3.

Table 1. The dimensions of the six study samples.

	Sample 1	Sample 2	Sample 3	Sample 4	Sample 5	Sample 6
Gate length (L_G, μm)	40	40	40	40	40	40
Gate edge size (L_{Edge}, μm)	–	–	–	3	3	3
Total channel width (W, μm)	100	100	100	100	100	100
Gap width (W_{Gap}, μm)	3	3	3	3	3	3
Gap angle (α, °)	0	30	60	0	30	60
Gate-source distance (L_{GS}, μm)	5	5	5	5	5	5
Gate-drain distance (L_{GD}, μm)	5	5	5	5	5	5

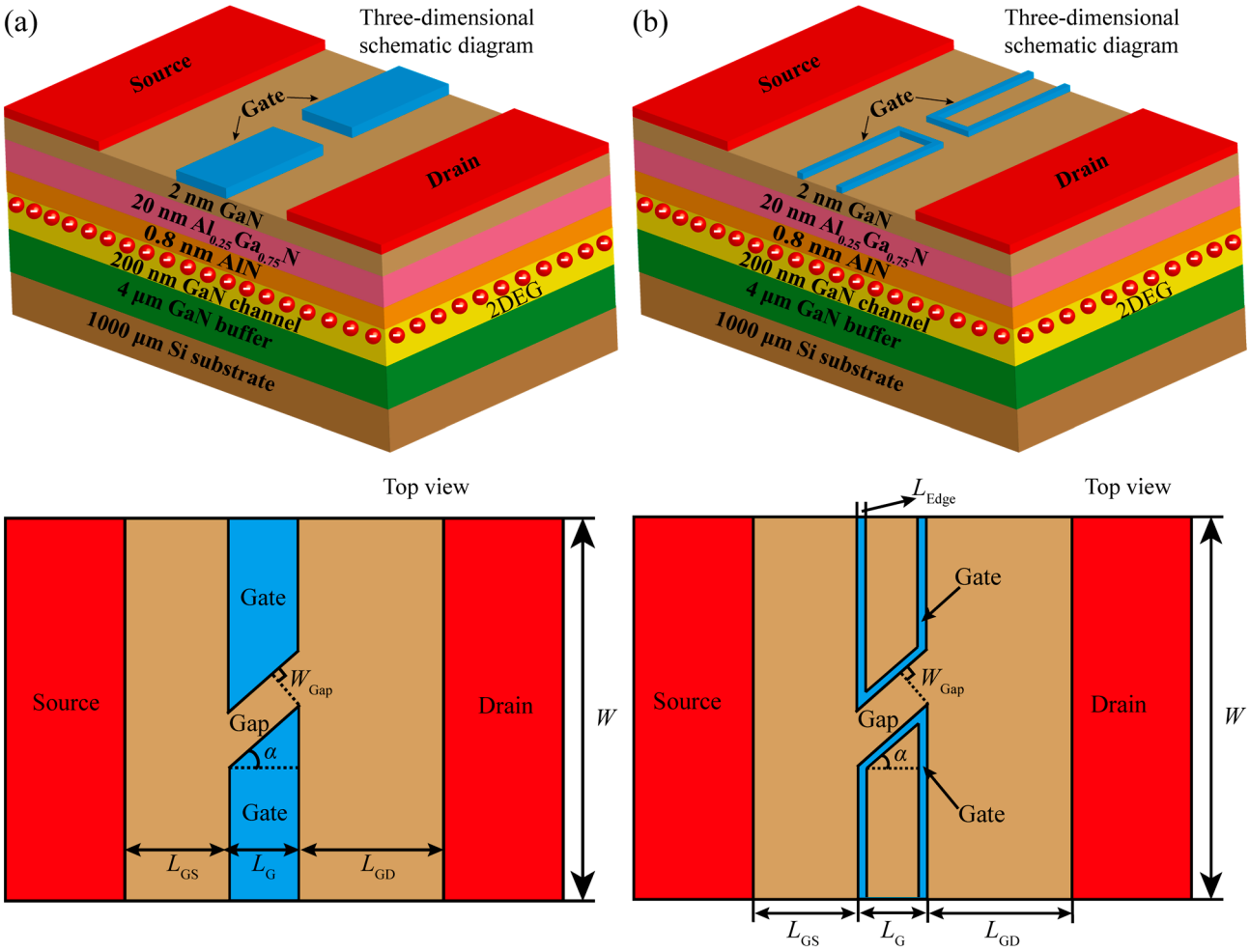


Figure 1. Schematic diagram of (**a**) SG and (**b**) HSG AlGaN/GaN HFETs.

3. Results and Discussion

3.1. Analysis of Measured Electrical Characteristics of SG Samples

The results of I-V output measurements for samples 1–3 are shown in Figure 2. As can be seen from Figure 2a–c, during the process of reducing the gate bias from 0 to −4.5 V, all three samples exhibited typical characteristics of SG AlGaN/GaN HFETs. Within the gate bias range of −3.5 to 0 V, the drain–source current (I_{DS}) declines as the gate–source voltage (V_{GS}) decreases, showing strong gate-controlled modulation. At this time, the channel underneath the gate is not yet pinched off, and the modulation of n_{2D} underneath the gate by V_{GS} is the dominant mechanism governing the variation in I_{DS}. When V_{GS} is lower than −3.5 V, the channel current is not turned off and can still be modulated by the gate bias, but the modulation capability is significantly weakened. This indicates that the channel underneath the gate is basically pinched off when $V_{GS} < -3.5$ V, and the current is then conducted between the source and drain electrodes through the gap region, with the dominant current modulation mechanism changing to PCF scattering [14]. The gate fringe electric field also contributes to current modulation, yet its influence is weak relative to PCF scattering when W_{Gap} is on the micrometer scale. Based on the modulation mechanisms discussed above, the effect of PCF scattering should be strengthened to ensure V_{GS} effectively modulates I_{DS} after the gated channel is pinched off. Increasing the gate length is a simple and efficient approach to enhance PCF scattering; this justifies the adoption of a large gate length in this work.

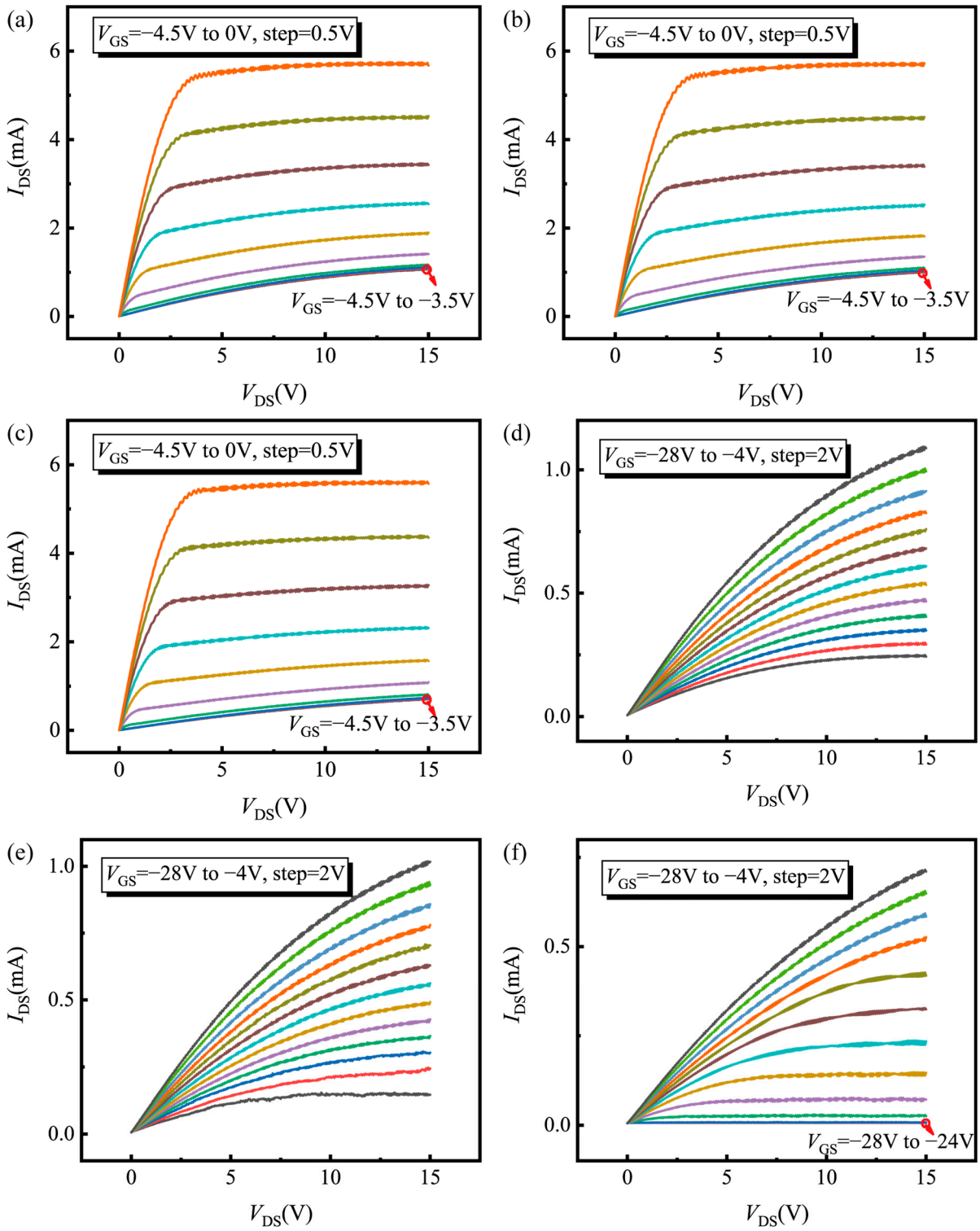


Figure 2. The measured I-V output characteristics of samples (**a**) 1, (**b**) 2, and (**c**) 3 at V_{GS} = −4.5 to 0 V and of samples (**d**) 1, (**e**) 2, and (**f**) 3 at V_{GS} = −28 to −4 V.

To more accurately extract the gate-channel pinch-off voltage (V_P) for samples 1–3, their C-V curves were measured, with the results shown in Figure 3a. Due to the different gap angles, the gate areas of samples 1–3 are different, leading to differences in their capacitance values. Sample 3 has the smallest gate area and thus the smallest capacitance, while the gate area of sample 1 is slightly larger than that of sample 2, resulting in an insignificant difference in their capacitance values. The V_P for SG samples can be approximately

determined based on the step voltage of the C-V curve [14]. As can be seen from Figure 3a, the capacitances of samples 1–3 decrease rapidly to a minimal value around V_{GS} = −4 V, from which the V_P for the three samples is approximately derived as −4 V. In the above discussion of the I-V output characteristics of samples 1–3, we noted that the gated channel seemed to be pinched off at V_{GS} = −3.5 V, which is inconsistent with the V_P extracted from the C-V curves. This is because when V_{GS} = −3.5 V, although the electrons in the gate region are not depleted, n_{2D} is much lower than that in the gap region. At this time, the total channel current of the samples is mainly composed of the current in the gap region, and the variation in n_{2D} in the gate region, caused by the gate bias, has a negligible effect on this. Therefore, in the V_{GS} range of −3.5 to −4 V, the I-V output characteristic curves of samples 1–3 exhibit weak modulation, which is consistent with the characteristics after the pinch-off of the gated channel, leading to an erroneous determination of the V_P. This also indicates that the V_P extracted from the C-V characteristic curves is more accurate.

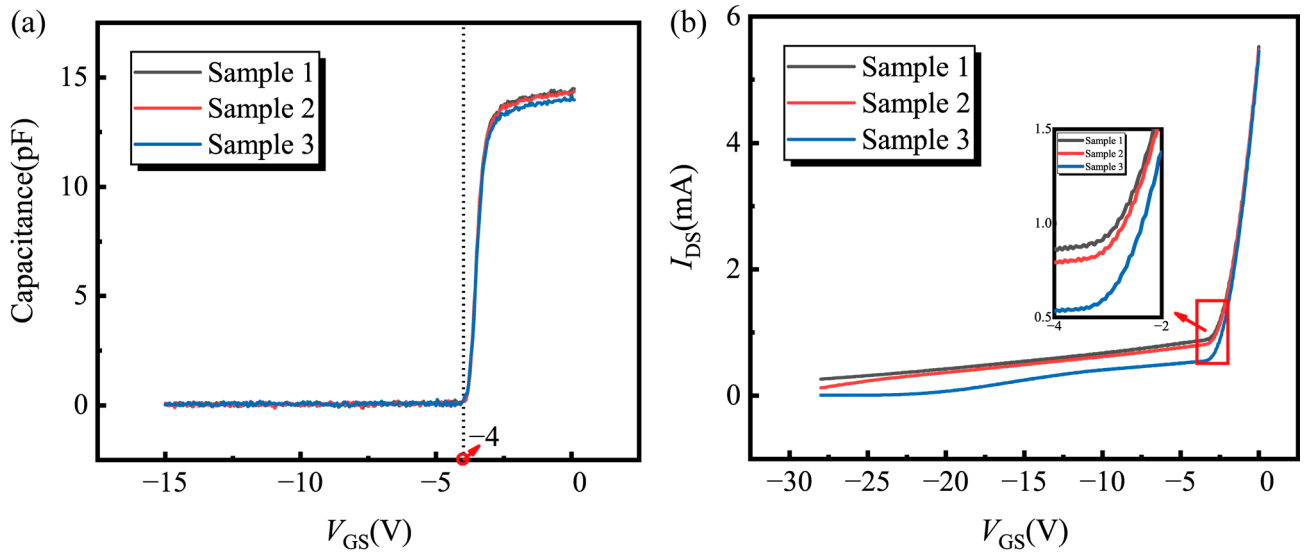


Figure 3. The measured (**a**) C-V and (**b**) transfer characteristics of samples 1–3.

To further study the variation in I_{DS} with V_{GS} after the depletion in electrons underneath the gate, we adjusted the range and step of V_{GS} during measurement of the I-V output characteristics; the obtained curves are shown in Figure 2d–f. It can clearly be seen that after the pinch-off of the gated channel, the modulation of I_{DS} by V_{GS} is still effective despite the extremely weak modulation capability. Comparing Figure 2d–f, it can be observed that sample 3 is essentially turned off at V_{GS} = −24 V, while samples 1 and 2 cannot be turned off even when V_{GS} is reduced to −28 V. However, although neither of the two samples is turned off, the I_{DS} of sample 2 at V_{GS} = −28 V is closer to the turn-off state than that of sample 1. This means that, for samples 1–3, a larger gap angle makes it easier to turn off the devices. It should be mentioned that the turn-off state defined in this work differs from the condition where the gated channel is pinched off; it instead refers to the state in which the residual gap-region current is suppressed.

When the drain–source voltage (V_{DS}) was 10 V, the transfer characteristics of the samples were measured and are plotted in Figure 3b. The transfer curves of samples 1 and 2 are clearly divided into strong- and weak-modulation regions before and after the gate pinch-off point, respectively, while sample 3 exhibits an additional current turn-off region beyond these two regions. All these features are consistent with those observed in the I-V output characteristics. After the channel underneath the gate is pinched off, at a given gate bias, I_{DS} decreases as the gap angle increases. The main reason for this trend is straightforward: a larger gap angle directly increases the length of the gap region, raising

the overall channel resistance and reducing I_{DS}. Notably, this trend holds even in some gate bias ranges before the gated channel is pinched off. This behavior is interesting and seemingly counterintuitive. For a sample with a larger gap angle, the gate area is smaller, so fewer 2DEG electrons are consumed under the same negative gate bias. If current flows uniformly parallel from drain to source, devices with less electron consumption should carry larger currents, which contradicts the measured results. This finding indicates that, as electrons underneath the gate are reduced, the 2DEG concentration profile in the channel changes and the electron flow direction is no longer completely parallel to the channel even before the gate pinch-off point, but bends in accordance with the gap angle. This bending lengthens the current path in devices with larger gap angles, resulting in lower current. Although the origins of current bending reported by N. B. Schade et al. may differ from those discussed in this work, they also reported the phenomenon that current propagates along bent paths within straight wire [21]. This may serve as indirect supportive evidence for the above conclusion.

The transconductance (g_m) of each sample can be obtained by differentiating the transfer curve, enabling quantitative comparison of current modulation strength among different samples. However, as shown in Figure 3b, the transfer curves of the three samples are not sufficiently smooth, so direct differentiation fails to yield reliable transconductance values. This non-smooth nature of the measured I-V curves (Figures 2 and 3b) is attributed to the saturation mechanism of SG devices [20,22]. Since the gap region of an SG device is not covered by the gate, the current through the gap cannot saturate via the conventional channel saturation mechanism. Instead, saturation is attained via the virtual gate or device self-heating [22–26]. The velocity saturation originating from self-heating requires an extremely high drain–source electric field, which cannot be achieved within the V_{DS} range adopted in this work. On the other hand, the formation of a virtual gate relies on electron trapping by surface trap states, making it difficult to establish a virtual gate with stable potential. Fluctuations in the virtual gate potential consequently induce current variations, which ultimately result in non-smooth I-V characteristics. Introducing an auxiliary gate in the gate–drain region can significantly improve the saturation characteristics of SG devices [22], but such a structure was not used in this work to simplify the theoretical analysis.

As shown in the above analysis, direct differentiation of the transfer curves to calculate transconductance is impractical. To quantitatively compare the current modulation capabilities of the three samples, a fitting method was used to approximate the average transconductance over selected V_{GS} ranges. Specifically, linear fitting is performed on the transfer curve in a nearly linear interval, and the slope of the fitted line is taken as the average transconductance for that range. This approach improves accuracy by restricting fits to linear segments. The results are listed in Table 2. Before the channel underneath the gate is pinched off, the transconductances follow $g_{m1} < g_{m2} < g_{m3}$, matching the trend in Figure 3b. Thus, a larger gap angle enhances the gate-controlled modulation in SG samples. The physical origin is clear: within the selected V_{GS} range, the transfer curves are approximately linear, so their slopes can be approximately considered to be mainly determined by the current values at the two endpoints. Samples 1–3 share an identical material structure, device geometry, and dimensions, except for the gap angle, so their I_{DS} values are very similar at $V_{GS} = 0$ V. As seen in Figure 3b, at $V_{GS} = -2.5$ V, I_{DS} is lower for samples with larger gap angles, as explained earlier. Consequently, before the 2DEG electrons underneath the gate are depleted, samples with larger gap angles exhibit higher transconductance in the chosen V_{GS} range. After the gate pinch-off point, the transconductances of samples 1–3 show no clear systematic dependence on gap angle. The I_{DS} in the gate-free region is governed by multiple factors, primarily the gate fringe electric field,

PCF scattering, and W_{eff} [14,18,27]. In addition, because the transfer curves in Figure 3b were measured in the saturation region, the surface virtual gate also affects I_{DS}. Due to the combined influence of these various factors, it is difficult for the transconductance to exhibit regular changes with varying gap angles.

Table 2. The approximate average values of calculated g_m for samples 1–3.

	g_m (S)		
	Sample 1	**Sample 2**	**Sample 3**
$-2.5\ V \leq V_{GS} \leq 0\ V$	1.75×10^{-3}	1.77×10^{-3}	1.84×10^{-3}
$-20\ V \leq V_{GS} \leq -4\ V$	2.70×10^{-5}	2.63×10^{-5}	2.99×10^{-5}

3.2. Analysis of the Conduction Channel Effective Width Using HSG Samples

According to our previous work on SG AlGaN/GaN HFETs, after the 2DEG electrons underneath the gate are depleted, the conduction width of the channel in gate–source and gate–drain regions differs from the physical gap width [18,20,27]. To simplify the quantitative analysis, the entire conduction channel is modeled as a rectangular region, whose width is defined as W_{eff}. For SG AlGaN/GaN HFETs, the structure and size of the devices can affect W_{eff} [18,27]. It is difficult to quantitatively determine W_{eff} directly via experimental methods; to determine this value requires the use of an HSG structure [20].

The C-V characteristics of HSG samples 4–6 are plotted in Figure 4a. For HSG samples, a larger gap angle corresponds to a larger gate area, in contrast to SG devices. Accordingly, capacitance increases with the gap angle, as shown in Figure 4a. The gate pinch-off voltage of HSG samples is also approximated from the step voltage in the C-V curve. Since all samples are grown on the same material, their gate pinch-off voltages are theoretically identical, and extraction from the C-V curves confirms this value to be −4 V for all samples. With the gate pinch-off point identified for HSG samples, the I-V characteristics at this bias were obtained, as shown in Figure 4b. After the electrons underneath the gate of the HSG samples are depleted, I_{DS} decreases as the gap angle increases, which is similar to what was observed for the SG samples. The most direct cause is the increased gap region length, associated with a larger gap angle. In addition, variations in the gap angle may alter W_{eff}, which constitutes one of the factors influencing I_{DS}.

At $V_{GS} = V_P$, the influence of the gate fringe electric field on electrons in the gap region is negligible [7,8,14], so W_{eff} can be determined under this condition. For a sample with a gap angle of 0, based on previous research, W_{eff} can be expressed as [20]

$$W_{eff} = \frac{L_{DS}}{n_{2D} e \mu_{Total} R_{DS}}. \quad (1)$$

Here, e represents the absolute value of electron charge and μ_{Total} is the total electron mobility of the conduction channel. For HSG samples, at the gate pinch-off point, n_{2D} and μ_{Total} in the gate-free region are approximately identical to those of the AlGaN/GaN heterostructure material [20]. R_{DS} is the total conduction channel resistance and can be derived from the I-V characteristics of HSG samples under low-field conditions.

For samples with a non-zero gap angle, the physical length of the conduction channel is no longer L_{DS}, and the length of the equivalent rectangular channel (L_{eff}) must be adjusted accordingly. The generalized expression for W_{eff} can then be rewritten as

$$W_{eff} = \frac{L_{eff}}{n_{2D} e \mu_{Total} R_{DS}}. \quad (2)$$

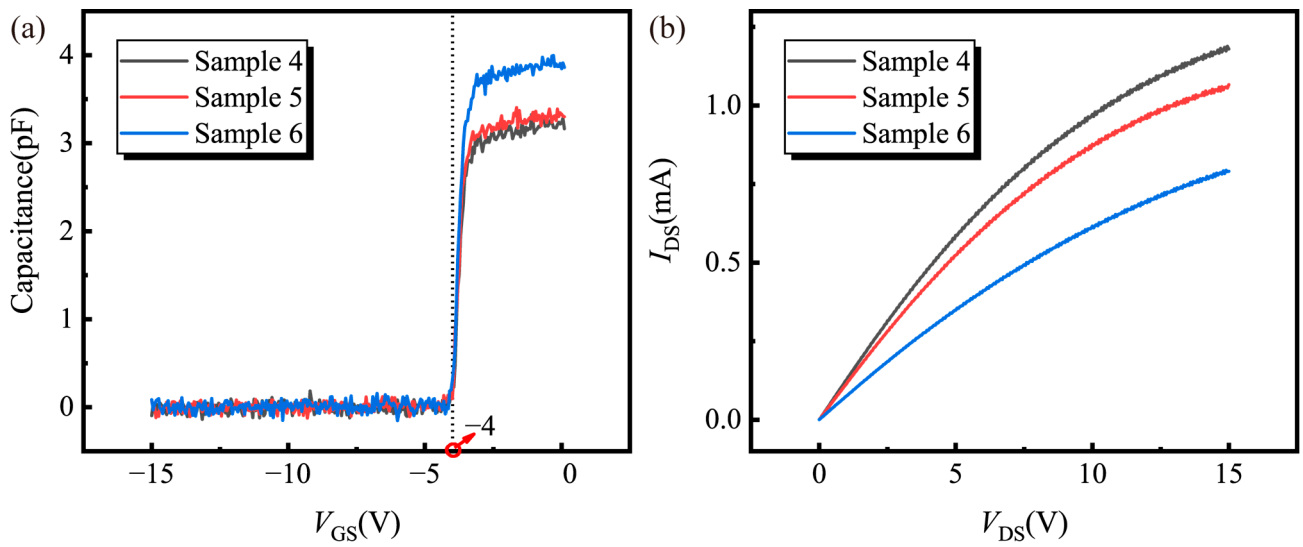


Figure 4. The measured (**a**) C-V characteristics and (**b**) I-V characteristics at V_{GS} = −4 V of HSG samples 4–6.

Here, L_{eff} satisfies $L_{eff} = L_{GS} + L_{GD} + L_G/\cos\alpha$, where α is the gap angle.

Calculations yield W_{eff} values of approximately 3.214 μm, 3.113 μm, and 2.845 μm for samples 4–6, respectively. It can be seen that W_{eff} decreases as the gap angle increases. Two mechanisms may account for this trend. First, a larger gap angle reduces the number of 2DEG electrons available for conduction in the gate–source and gate–drain regions, increasing the series resistance of these regions and reducing W_{eff}. Second, a larger gap angle distorts the electron transport path into a more curved trajectory. In contrast with a straight channel, the electron velocity may be altered in a curved channel, increasing overall channel resistance. This resistance rise actually originates from degraded electron mobility, but μ_{Total} is assumed to be constant in the derivation of W_{eff}. The increased channel resistance is therefore reflected as a reduction in W_{eff}. Based on the present experimental data, it is difficult to distinguish which mechanism dominates or whether both contribute simultaneously. Nevertheless, both mechanisms demonstrate that the geometric shape of the conduction channel affects current transport. This geometric effect will be investigated in detail in future work.

3.3. Analysis of Transport Characteristics in SG Samples Based on PCF Scattering

PCF scattering arises from the strong polarization effect in GaN-based materials and is a characteristic scattering mechanism in GaN-based HFETs [28–33]. In AlGaN/GaN heterostructure materials, the polarization charge distribution at the interface is almost uniform; thus, PCF scattering is negligible. In AlGaN/GaN HFETs, application of a gate bias renders the polarization charge distribution non-uniform via the inverse piezoelectric effect, inducing PCF scattering [28,34]. For SG AlGaN/GaN HFETs, after the gate pinch-off point, the PCF scattering mainly reflects the interaction between the additional polarization charges beneath the gate and the 2DEG electrons in the conduction channel [14,27]. This interaction is described by the PCF scattering potential, given as [14,27,35]

$$V(x,y,z) = -\frac{e}{4\pi\varepsilon_s\varepsilon_0}\iint_G \frac{\sigma_G}{\sqrt{(x-x')^2+(y-y')^2+z^2}}dx'dy'. \quad (3)$$

Here, ε_0 and ε_s are the dielectric permittivity and static dielectric constant of GaN, respectively. The integration domain G corresponds to the gate region of the SG devices, and σ_G denotes the additional polarization charge density underneath the gate.

Affected by the PCF scattering potential, electrons in the conduction channel are scattered from an initial state $\boldsymbol{k}$ to a final state $\boldsymbol{k'}$. This process is described by the matrix element as [14,27,35,36]

$$\begin{aligned} M_{k\to k'} &= A^{-1}\int_0^{\infty}\psi_{k'}^{*}(z) \\ &\times\left[\int_{-\frac{Leff}{2}}^{\frac{Leff}{2}}dx\int_{\frac{W-W_{eff}}{2}}^{\frac{W+W_{eff}}{2}}V(x,y,z)\exp\left(-iq_x x-iq_y y\right)dy\right]\psi_k(z)dz \\ &= A^{-1}\int_0^{\infty}\psi_{k'}^{*}(z)\left[V\left(q_x,q_y,z\right)\right]\psi_k(z)dz. \end{aligned} \tag{4}$$

In Equation (4), A represents the two-dimensional normalization constant. $\psi(z) = \left(b^3z^2/2\right)^{1/2}\exp(-bz/2)$ denotes the Fang–Howard variational wave function associated with 2DEG electrons, where $b = \left(33m^*e^2n_{2D}/8\varepsilon_0\varepsilon_s\hbar^2\right)^{1/3}$ is the variational parameter, m^* is the electron effective mass of the GaN material, and $\hbar$ is the reduced Planck constant. Since all electrons involved in the relevant calculations reside within the ungated region, the material's measured n_{2D} is adopted in calculations herein and subsequent derivations. q_x and q_y correspond to the projections of the wave-vector variation $\boldsymbol{q} = \boldsymbol{k'} - \boldsymbol{k}$ along the x and y axes, respectively. The wave-vector variation $\boldsymbol{q}$ satisfies $q = \left|2\left(2m^*\hbar^{-2}E\right)^{1/2}\sin(\theta/2)\right|$, where E is the 2DEG electron energy, and θ is the scattering angle of the 2DEG electron from $\boldsymbol{k}$ to $\boldsymbol{k'}$.

Since the actual shape of the conduction channel is unknown, an equivalent rectangular channel with a length of L_{eff} and a width of W_{eff} is used for approximations in Equation (4). It should be noted that W_{eff} is obtained at $V_{\text{GS}} = -4$ V, where the channel underneath the gate is just pinched off and the gate fringe electric field is negligible. When $V_{\text{GS}} < -4$ V, the fringe electric field effect emerges, which leads to depletion of electrons in the channels on both sides of the gap, thereby narrowing the gap region and further affecting the effective width of the entire channel [14]. Unfortunately, existing methods cannot reliably determine W_{eff} with fringe electric field effects included. Also considering the above discussion that the fringe electric field exerts a much weaker impact than PCF scattering, its contribution is neglected in subsequent calculations as a necessary simplification. This approximation would introduce certain errors, especially when V_{GS} deviates significantly from -4 V. Since the effect of the fringe electric field is a reduction in W_{eff}, such a simplification tends to overestimate W_{eff} and accordingly yield lower calculated values of μ_{PCF}. Although quantitative accuracy is limited by the aforementioned errors, the calculation results remain valid for a qualitative comparison among samples 1–3 under identical approximation conditions.

Once the matrix element is determined, the derivations concerning PCF scattering can be performed following a standard analytical workflow (Supplementary Section S1) [35–40]. The electron mobilities associated with PCF scattering for samples 1–3 at various V_{GS} values were computed via a self-consistent iterative procedure [40], and the results are plotted in Figure 5. For all three samples, the mobility decreases with decreasing V_{GS}. Under negative gate bias, a lower V_{GS} corresponds to a larger absolute value of V_{GS}. Based on the inverse piezoelectric effect, a larger absolute value of V_{GS} increases the additional polarization charge density underneath the gate, strengthening PCF scattering and reducing μ_{PCF}. Comparison of the μ_{PCF}–V_{GS} curves for samples 1–3 reveals no clear systematic dependence of the PCF scattering intensity on gap angle. An isolated comparison of samples 1 and 2 might suggest that μ_{PCF} increases with gap angle, but sample 3 breaks this trend. We attempt to explain the origin of this irregular variation in the following.

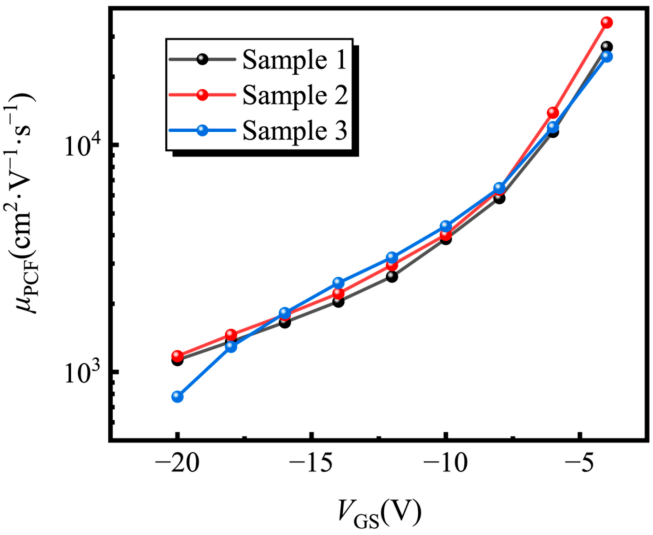


Figure 5. The calculated μ_{PCF} for samples 1–3 as a function of V_{GS}.

On the one hand, the gap angle modulates the total amount of additional polarization charges. With all other structural and dimensional parameters fixed, a larger gap angle reduces the total gate area, directly lowering the total amount of additional polarization charges in the gate region. According to Equation (3), the PCF scattering potential decreases accordingly, ultimately leading to an attenuation in PCF scattering and an increase in μ_{PCF}. On the other hand, the gap angle changes the spatial distribution of additional polarization charges. As the gap angle increases, the entire gap region lengthens; thus, more additional polarization charges accumulate adjacent to both sides of the gap, which lie closest to the gap region. Since PCF scattering is essentially Coulomb scattering, charges closer to the channel electrons produce stronger scattering, as implied by Equation (3). The increased additional polarization charge near the gap thus enhances PCF scattering and reduces μ_{PCF}. In summary, the gap angle affects both the total amount and the spatial distribution of additional polarization charges, and these two effects have an opposing influence on PCF scattering. When the total-charge effect dominates, μ_{PCF} increases with the gap angle; when the distribution effect dominates, the opposite occurs. As a result, the PCF scattering intensity shows no overall regular dependence on gap angle.

4. Conclusions

In summary, a series of SG AlGaN/GaN HFETs with different gap angles were fabricated and characterized to explore the influence of the gap angle on their transport characteristics. The I-V characteristics demonstrated that the gap angle affects the turn-off voltage of SG samples, with a larger gap angle corresponding to a higher turn-off voltage. Further analysis of the transfer characteristics showed that the gap angle alters the current flow path even before the pinch-off of the gated channel, thus regulating I_{DS}. W_{eff} values were quantitatively determined using HSG samples, and it was found that W_{eff} decreases as the gap angle increases. In addition, the μ_{PCF} of SG samples at various V_{GS} values was quantitatively calculated under reasonable approximations. It was revealed that the gap angle affects PCF scattering through two competing mechanisms: a larger gap angle reduces the total amount of additional polarization charges and weakens PCF scattering, while it also reshapes the charge distribution to enhance PCF scattering. As a result, μ_{PCF} exhibits no regular dependence on the gap angle. This work provides new insights into the structural design and performance optimization of SG AlGaN/GaN HFETs, and the identified geometric effect is worthy of in-depth investigation in future work.

Supplementary Materials: The following supporting information can be downloaded at: https://www.mdpi.com/article/10.3390/mi17070831/s1, Section S1: The standard PCF scattering theoretical model and related formulas after determining the matrix element.

Author Contributions: Conceptualization, Y.L.; methodology, G.J., C.F. and Y.L.; validation, Y.L.; investigation, Y.K. and X.Z.; resources, C.L.; writing—original draft preparation, Y.K.; writing—review and editing, Y.K. and Y.L.; supervision, Z.H. and G.Z.; funding acquisition, Y.L. All authors have read and agreed to the published version of the manuscript.

Funding: This work was supported by the National Natural Science Foundation of China (Grant No. 12404090), the Natural Science Foundation of Shandong Province (Grant No. ZR2023QF120), and the Scientific Research Fund of Shandong Jiaotong University (Grant No. Z202322).

Institutional Review Board Statement: Not applicable.

Informed Consent Statement: Not applicable.

Data Availability Statement: The data that support the findings of this study are available from the corresponding author upon reasonable request.

Conflicts of Interest: The authors declare no conflict of interest.

References

1. Muktadir, M.S.; Ahmad, M.A.; Mech, B.C. Recent Innovations in GaN HEMT Fabrication for Enhanced High-Frequency Performance: A Review. *J. Electron. Mater.* **2026**, *55*, 3987–4004. [CrossRef]
2. Xiong, Y.; Sadek, M.; Chu, R. Recent advances in GaN-based power devices and integration. *Semicond. Sci. Technol.* **2025**, *40*, 033002. [CrossRef]
3. Chen, J.; Seshadri, P.; Stephenson, K.; Mamun, M.A.; Bai, R.; Wang, Z.; Khan, A.; Gupta, C. 64% AlGaN Channel HFET with High Johnson's Figure of Merit (>6 THz·V). *IEEE Electron Device Lett.* **2025**, *46*, 545–548. [CrossRef]
4. Wang, M.; Lv, Y.; Zhou, H.; Liu, C.; Cui, P.; Huang, S.; Lin, Z. Electron Velocity Modulation and Short-Channel Effect Impact on High-Frequency Performance in Sub-100 nm AlGaN/GaN HFETs. *IEEE Trans. Electron Devices* **2026**, *73*, 117–123. [CrossRef]
5. Wang, M.; Lv, Y.; Zhou, H.; Liu, C.; Cui, P.; Lin, Z. Impact of electron velocity modulation on microwave power performance for AlGaN/GaN HFETs. *Appl. Phys. Lett.* **2024**, *125*, 202105. [CrossRef]
6. Li, N.D.; Lin, Y.C.; Chen, K.W.; Hsu, H.T.; Tsao, Y.F.; Chang, E.Y. Novel Gate Fabrication Process Enhancing High-Frequency Operation in AlGaN/GaN HEMTs for Ka-Band Applications. *IEEE J. Electron Devices Soc.* **2025**, *13*, 593–598. [CrossRef]
7. Thornton, T.J.; Pepper, M.; Ahmed, H.; Andrews, D.; Davies, G.J. One-Dimensional Conduction in the 2D Electron Gas of a GaAs-AlGaAs Heterojunction. *Phys. Rev. Lett.* **1986**, *56*, 1198–1201. [CrossRef] [PubMed]
8. Zheng, H.Z.; Wei, H.P.; Tsui, D.C.; Weimann, G. Gate-controlled transport in narrow GaAs/AlxGa1-xAs heterostructures. *Phys. Rev. B* **1986**, *34*, 5635–5638. [CrossRef]
9. Spirito, D.; Frucci, G.; Di Gaspare, A.; Di Gaspare, L.; Giovine, E.; Notargiacomo, A.; Roddaro, S.; Beltram, F.; Evangelisti, F. Quantum transport in low-dimensional AlGaN/GaN systems. *J. Nanopart. Res.* **2011**, *13*, 5699–5704.
10. Blick, R.H.; Haug, R.J.; Weis, J.; Pfannkuche, D.; Klitzing, K.V.; Eberl, K. Single-electron tunneling through a double quantum dot: The artificial molecule. *Phys. Rev. B* **1996**, *53*, 7899–7902. [CrossRef]
11. Moon, J.S.; Blount, M.A.; Simmons, J.A.; Wendt, J.R.; Lyo, S.K.; Reno, J.L. Magnetoresistance of one-dimensional subbands in tunnel-coupled double quantum wires. *Phys. Rev. B* **1999**, *60*, 11530–11534. [CrossRef]
12. Kumar, A.S.; Garigapati, N.S.; Saha, D. Low field mobility in electrostatically evolved AlGaN/GaN one-dimensional channel from a two-dimensional electron gas system. *Appl. Phys. Lett.* **2019**, *115*, 032105. [CrossRef]
13. Surapaneni, S.; Jha, J.; Pendem, V.; Yadav, Y.K.; Ganguly, S.; Saha, D. Low-field mobility in an electrostatically confined 2D rectangular nanowire: Effect of density of states and phonon confinement. *Nanotechnology* **2021**, *32*, 455202. [CrossRef]
14. Liu, Y.; Lv, Y.; Guo, S.; Luan, Z.; Cheng, A.; Lin, Z.; Yang, Y.; Jiang, G.; Zhou, Y. A novel AlGaN/GaN heterostructure field-effect transistor based on open-gate technology. *Sci. Rep.* **2021**, *11*, 22431. [CrossRef] [PubMed]
15. Zhou, H.; Lv, Y.; Liu, Y.; Wang, M.; Cui, P.; Lin, Z. Study on the frequency characteristics of split-gate AlGaN/GaN HFETs. *Mod. Phys. Lett. B* **2024**, *38*, 2450092.
16. Zhou, H.; Lv, Y.; Liu, C.; Yang, M.; Lin, Z.; Liu, Y.; Wang, M. Study of electrical transport properties in split-gate AlGaN/GaN heterostructure field-effect transistors. *Solid-State Electron.* **2024**, *212*, 108833. [CrossRef]
17. Zhou, H.; Zhama, T.; Wang, M.; Lin, Z.; Zeng, Y.; Cui, P. High-field electron transport and current saturation mechanism of open region channel in submicron split-gate AlGaN/GaN HFETs. *J. Phys. D Appl. Phys.* **2025**, *58*, 135108. [CrossRef]

18. Liu, Y.; Lv, Y.; Lin, Z.; Yang, Y.; Jiang, G.; Zhou, Y. A submicron split-gate AlGaN/GaN heterostructure field-effect transistor for class-A common-source voltage amplifier applications. *Micro Nanostruct.* **2022**, *168*, 207319. [CrossRef]
19. Lee, S.; Kim, Y.J.; Yoo, H. Split-Gate: Harnessing Gate Modulation Power in Thin-Film Electronics. *Micromachines* **2024**, *15*, 164. [CrossRef] [PubMed]
20. Liu, Y.; Kang, Y.; Jiang, G.; Fu, C.; Zhang, G.; Yang, G.; Luan, C.; Yang, M. A novel method to determine the conduction channel effective width of split-gate AlGaN/GaN high electron mobility transistors. *AIP Adv.* **2025**, *15*, 115223. [CrossRef]
21. Schade, N.B.; Schuster, D.I.; Nagel, S.R. A nonlinear, geometric Hall effect without magnetic field. *Proc. Natl. Acad. Sci. USA* **2019**, *116*, 24475–24479. [CrossRef] [PubMed]
22. Liu, Y.; Lv, Y.; Zhou, H.; Lin, Z.; Yang, Y.; Jiang, G.; Zhou, Y.; Wang, M. A split-gate AlGaN/GaN heterostructure field-effect transistor with an auxiliary gate. *AIP Adv.* **2022**, *12*, 025012. [CrossRef]
23. Vitusevich, S.A.; Danylyuk, S.V.; Klein, N.; Petrychuk, M.V.; Avksentyev, A.Y.; Sokolov, V.N.; Kochelap, V.A.; Belyaev, A.E.; Tilak, V.; Smart, J.; et al. Separation of hot-electron and self-heating effects in two-dimensional AlGaN/GaN-based conducting channels. *Appl. Phys. Lett.* **2003**, *82*, 748–750. [CrossRef]
24. Ardaravičius, L.; Matulionis, A.; Liberis, J.; Kiprijanovic, O.; Ramonas, M.; Eastman, L.F.; Shealy, J.R.; Vertiatchikh, A. Electron drift velocity in AlGaN/GaN channel at high electric fields. *Appl. Phys. Lett.* **2003**, *83*, 4038–4040. [CrossRef]
25. Kuzmík, J.; Bychikhin, S.; Pogany, D.; Gaquière, C.; Morvan, E. Current conduction and saturation mechanism in AlGaN/GaN ungated structures. *J. Appl. Phys.* **2006**, *99*, 123720. [CrossRef]
26. Tao, Q.; Wang, J.; Bin, Z.; Wang, X.; Li, M.; Cao, Q.; Wu, W.; Ma, X. Investigation on mechanisms of current saturation in gateless AlGaN/GaN heterostructure device. *Jpn. J. Appl. Phys.* **2021**, *60*, 020908. [CrossRef]
27. Liu, Y.; Fu, C.; Jiang, G.; Zhang, G.; Yang, G.; Lv, Y.; Lin, Z. Effect of device size on conduction channel effective width and polarization Coulomb field scattering intensity of split-gate AlGaN/GaN heterostructure field-effect transistors. *J. Appl. Phys.* **2023**, *134*, 165703. [CrossRef]
28. Zhao, J.; Lin, Z.; Corrigan, T.D.; Wang, Z.; You, Z.; Wang, Z. Electron mobility related to scattering caused by the strain variation of AlGaN barrier layer in strained AlGaN/GaN heterostructures. *Appl. Phys. Lett.* **2007**, *91*, 173507. [CrossRef]
29. Lv, Y.; Lin, Z.; Zhang, Y.; Meng, L.; Luan, C.; Cao, Z.; Chen, H.; Wang, Z. Polarization Coulomb field scattering in AlGaN/AlN/GaN heterostructure field-effect transistors. *Appl. Phys. Lett.* **2011**, *98*, 123512. [CrossRef]
30. Jiang, G.; Cui, P.; Fu, C.; Lv, Y.; Yang, M.; Cheng, Q.; Liu, Y.; Zhang, G. Influence of the Bias Voltage on Effective Electron Velocity in AlGaN/GaN High Electron Mobility Transistors. *Micromachines* **2024**, *15*, 1148. [CrossRef] [PubMed]
31. Wang, M.; Lv, Y.; Zhou, H.; Cui, P.; Liu, C.; Lin, Z. Bias-Dependent Electron Velocity Extracted From AlGaN/GaN HFETs and Its Impact on gm and fT. *IEEE Electron Device Lett.* **2024**, *45*, 160–163. [CrossRef]
32. Wang, M.; Zhou, H.; Liu, C.; Lin, Z.; Zeng, Y.; Cui, P. Bias-dependent electron velocity and short-channel effect in scaling sub-100 nm InAlN/GaN HFETs. *Appl. Phys. Lett.* **2024**, *124*, 152101. [CrossRef]
33. Lin, Z.; Zhou, H.; Lv, Y.; Cui, P.; Wang, M.; Luan, C.; Zhao, J.; Yang, M.; Fu, C. Effect of polarization Coulomb field scattering on GaN devices. *Appl. Phys. Rev.* **2026**, *13*, 011302. [CrossRef]
34. Anwar, A.F.M.; Webster, R.T.; Smith, K.V. Bias induced strain in AlGaN/GaN heterojunction field effect transistors and its implications. *Appl. Phys. Lett.* **2006**, *88*, 203510. [CrossRef]
35. Luan, C.; Lin, Z.; Lv, Y.; Zhao, J.; Wang, Y.; Chen, H.; Wang, Z. Theoretical model of the polarization Coulomb field scattering in strained AlGaN/AlN/GaN heterostructure field-effect transistors. *J. Appl. Phys.* **2014**, *116*, 044507. [CrossRef]
36. Gurusinghe, M.N.; Davidsson, S.K.; Andersson, T.G. Two-dimensional electron mobility limitation mechanisms in AlxGa1−xN/GaN heterostructures. *Phys. Rev. B* **2005**, *72*, 045316. [CrossRef]
37. Stern, F.; Howard, W.E. Properties of Semiconductor Surface Inversion Layers in the Electric Quantum Limit. *Phys. Rev.* **1967**, *163*, 816–835. [CrossRef]
38. Jiang, G.; Lv, Y.; Lin, Z.; Yang, Y.; Liu, Y.; Guo, S.; Zhou, Y. Polarization Coulomb field scattering with the electron systems in AlGaN/GaN heterostructure field-effect transistors. *AIP Adv.* **2020**, *10*, 075212. [CrossRef]
39. Cui, P.; Mo, J.; Fu, C.; Lv, Y.; Liu, H.; Cheng, A.; Luan, C.; Zhou, Y.; Dai, G.; Lin, Z. Effect of Different Gate Lengths on Polarization Coulomb Field Scattering Potential in AlGaN/GaN Heterostructure Field-Effect Transistors. *Sci. Rep.* **2018**, *8*, 9036. [CrossRef] [PubMed]
40. Cui, P.; Lin, Z.; Fu, C.; Liu, Y.; Lv, Y. A method to determine electron mobility of the two-dimensional electron gas in AlGaN/GaN heterostructure field-effect transistors. *Superlattices Microstruct.* **2017**, *110*, 289–295. [CrossRef]

Disclaimer/Publisher's Note: The statements, opinions and data contained in all publications are solely those of the individual author(s) and contributor(s) and not of MDPI and/or the editor(s). MDPI and/or the editor(s) disclaim responsibility for any injury to people or property resulting from any ideas, methods, instructions or products referred to in the content.